On the amphidromic structure of inertial waves in a rectangular parallelepiped

2003 Fluid Dyn. Res. 33 373

(http://iopscience.iop.org/1873-7005/33/4/A08)

ELSEVIER

Fluid Dynamics Research 33 (2003) 373–401

FLUID DYNAMICS RESEARCH

On the amphidromic structure of inertial waves in a rectangular parallelepiped

Leo R.M. Maas*

Netherlands Institute for Sea Research, P.O. Box 59, 1790 AB Texel, The Netherlands

Accepted 26 August 2003
Communicated by T. Mullin

Abstract

Enclosed rotating homogeneous fluids support waves that are restored by Coriolis forces. These waves propagate obliquely through the fluid under a fixed angle with respect to the rotation axis which is set by the ratio of the frequency of the wave and the inertial frequency (twice the angular frequency of the tank). In the particular case that boundaries are either parallel, or perpendicular to the rotation axis, eigenmodes may be expected. An example is Kelvin's (1880) axial can. However, the spatial structure of these waves can still be quite complicated, as shown here for waves in a 'horizontal' rectangular parallelepiped. The container's rigid horizontal top and bottom surfaces allow for modal expansion in the vertical, each mode being governed by the 'inertial' analogs of surface Poincaré and Kelvin waves. Combining these, as in the Taylor problem of reflecting surface Kelvin waves, one finds both the eigenfrequencies as well as the typical amphidromic structure (phase lines circling around nodal points) of the resulting inertial wave pattern in dependence of the remaining two parameters: the horizontal and vertical aspect ratios. This entails the approximative determination of eigenvalues of an infinite matrix equation, obtained with the Proudman–Rao method. It appears that certain specific frequencies persist as eigenfrequency for different aspect ratios, albeit belonging to different eigenmodes. Surprisingly, these correspond to the eigenfrequencies of an infinitely long channel of waves *lacking* along-channel structure. Inertial wave patterns are presented by means of the amplitude and phase of the internal elevation field (related to the axial velocity component) and of the two horizontal velocity components. These reveal predominant anticyclonic turning of phase and currents; maximum elevation and current amplitudes detached from the solid walls; and, occasionally, a nearly sloshing type of response (nodal lines, instead of points).

PACS: 47:32

Keywords: Rotating fluid; Inertial waves; Amphidromes; Parallelepiped; Degeneracy

* Tel: +31-222-369419; fax: +31-222-319674.
E-mail address: maas@nioz.nl (L.R.M. Maas).

0169-5983/$30.00
doi:10.1016/j.fluiddyn.2003.08.003

1. Introduction

Apart from short potential waves, a host of long, rotationally modified gravity waves, such as Kelvin and Poincaré waves, feature in geophysical fluid dynamics (Krauss, 1973; LeBlond and Mysak, 1978; Hendershott, 1981; Hutter, 1993). In a homogeneous fluid these waves are 'external' in the sense that their maximum elevations are (formally) reached at the surface. On a rotating plane (of angular frequency Ω), such waves may, in the presence of non-uniform depth, be accompanied by Rossby waves, which are restored by a fluid column's tendency to conserve potential vorticity. One may thus have the impression that in a uniformly rotating, uniform depth, homogeneous fluid the former external gravity waves are the only low-frequency waves possible, their trapping to the boundary seemingly a necessity, imposed by the elliptic nature of the governing equation. However, this skips a class of 'internal' wave modes, which have maximum vertical displacements in the *interior* of the fluid, and which vanish at the surface. These waves, of frequencies below the inertial frequency, $f = 2\Omega$, exist by virtue of non-hydrostatic effects, are solely restored by Coriolis forces and are known as (elastoid) inertial, or gyroscopic waves (Kelvin, 1880; Bjerknes et al., 1933; Fultz, 1959). These should not be confused with the 'inertial waves' in the oceanographic literature, where this term is often used to designate rotationally modified internal gravity waves of frequencies slightly *above* or at the inertial frequency (Fu, 1981). The ellipticity 'constraint' of surface trapping is escaped since inertial waves are governed by a hyperbolic equation, Poincaré's equation (Greenspan, 1968). Inertial waves proper are often neglected in thin-fluid systems as ocean and atmosphere because they have small wave lengths, and because of the stratification of these media. The scale length of the inertial waves is the depth-scale of the vertical mode considered, which is therefore small, making the waves more susceptible to viscous degradation. Relative to this length scale, long waves thus appear only when their frequencies approach the inertial frequency f. However, for 'fat bodies' of fluid (Lighthill, 1966), like the earth core, stellar interiors and in some industrial applications, it is natural to consider these waves over a broader subinertial frequency range. Interestingly, suggestions on the oceanic relevance of inertial waves have recently appeared, based on observations in a well-mixed deep layer of the Meditteranean (van Haren and Millot, 2003).

Inertial waves were first discovered theoretically in an axial cylinder (Kelvin, 1880) that can be considered of finite height, owing to the axial periodicity of the solutions. The axial 'can' with or without concentric inner cylinder is still one of the two, fully confined geometries (containers) for which the governing hyperbolic equation with oblique-derivative boundary conditions has been exactly solved. The other container for which regular solutions are found is the axial spheroid (Bryan, 1889). A particular subclass of these solutions, the so-called toroidal modes, lacking radial displacements, also survive in the spherical shell (Malkus, 1967; Rieutord et al., 2000), but this denumerable set of regular waves co-exists with a continuum of singular (or focusing) waves that constitute the generic wave response in fluid-filled rotating containers (Rieutord et al., 2000). Indeed, since inertial waves propagate obliquely with respect to the rotation axis, any container having a side wall that is neither parallel nor perpendicular to the axis of rotation, and whose shape thus breaks the 'local reflectional symmetry', is prone to focus these waves (Phillips, 1963; Maas, 2001). In that respect, the spheroid is exceptional, because of its apparent ability to exactly compensate focusing reflections with defocusing reflections. From this point of view, only the occurrence of regular modes in the non-focusing, axial can could actually have been anticipated. Yet, within the class of non-focusing containers, owing to its axisymmetry, even this container is special as it lacks

the typical amphidromic structure: the presence of nodal points around which phase lines circle. The appearance of such amphidromic points will be discussed here by computing the inertial wave pattern in a rectangular parallelepiped: a cube stretched in two directions. Despite its innocuous shape, the rectangular parallelepiped does not seem to have been discussed with regards to inertial waves before. This container is non-focusing when its faces are again taken parallel or perpendicular to the rotation axis. The sensitiveness of the resulting regular wave pattern to the container's orientation can be anticipated from results in a slightly tilted, rectangular tank that is infinitely long in one horizontal direction (Høiland, 1962), and a corresponding sensitiveness to tilting of a cylindrical tank (Fultz, 1959; Wood, 1966; Scott, 1974; Thompson, 1979). Addition of an infinitesimal slope moreover opens the spectrum of Rossby waves.

Each of these theoretical results on inertial waves has been accompanied by observations, such as in the axial cylinder (Fultz, 1959; McEwan, 1970; Manasseh, 1992; Manasseh, 1996; Kobine, 1995), slightly tilted cylinder (Thompson, 1979), sphere (Aldridge and Toomre, 1969), tilted spheroid (Malkus, 1968; Vanyo et al., 1995), (truncated) cone (Beardsley, 1970), and, interestingly, in both the non-tilted and tilted rectangle (experiments by Fultz, discussed in Küchemann, 1965). Apart from verifying the predicted eigenfrequencies of inertial waves in an axial can (Fultz, 1959) and their oblique propagation (McEwan, 1970), these experiments typically show the long-time instability of the wave system (resonant collapse), variably attributed to resonant triad interactions (McEwan, 1971) supported by an observed subharmonic growth (Kobine, 1995), inertial instability (Kerswell, 1995; Lifschitz and Fabijonas, 1996), or centrifugal instabilities, owing to continued pumping and subsequent amplification of the standing wave pattern (Maas, 2001). The tank is often slightly tilted to produce perturbations at half the Coriolis frequency, but this set-up appears to generate remarkably strong mean flows too (Malkus, 1968; Manasseh, 1996; Thompson, 1979; Küchemann, 1965). Manasseh (1994), deeming second-order rectification of inertial waves in the boundary layer too weak to be responsible for a mean flow exceeding the flow associated with these waves, expressed the need for an amplification mechanism. It can be argued that geometric focusing of inertial waves, brought about by tilting of the boundaries, might just be such a mechanism. Observations of inertial waves in a tank of rectangular horizontal shape, having one sloping side wall, indeed not only shows the focusing of these waves, but also the generation of a mean flow at exactly the spot where the focusing was argued to be most prominent (Maas, 2001). A reinterpretation in terms of focusing inertial waves also seems warranted to explain the measured spectral response of inertial waves in the truncated cone (Beardsley, 1970; Maas et al., 1997). The observations (Maas, 2001; Manders and Maas, 2003) clearly require a theoretical description of inertial waves in a tilted rectangular parallelepiped (a 'box'). However, as inertial waves have not even been discussed in the non-tilted box, we here provide such a description in a *horizontal* box (Section 4). Contained inertial waves will appear as the final case of such waves considered in Section 3 in (1) an infinite layer, with rotation axis perpendicular to the rigid surface and bottom, (2) an infinite channel and (3) a half-infinite channel (see Fig. 1). The specialist reader may choose to skip Sections 3.1–3.4 altogether, as similar results can be found in the literature. We incorporate them here in order to make the text self-contained and to be able to draw the analogy to rotationally modified surface gravity waves, presenting the inertial waves as inertial Poincaré and Kelvin waves (Section 3). Yet, the waves considered here are purer in the sense that there is just one restoring mechanism involved, due to the Coriolis force. Consequently, in a box we need not consider the effect of varying the rotation 'strength' (the Coriolis frequency), as it is the only relevant frequency around. This

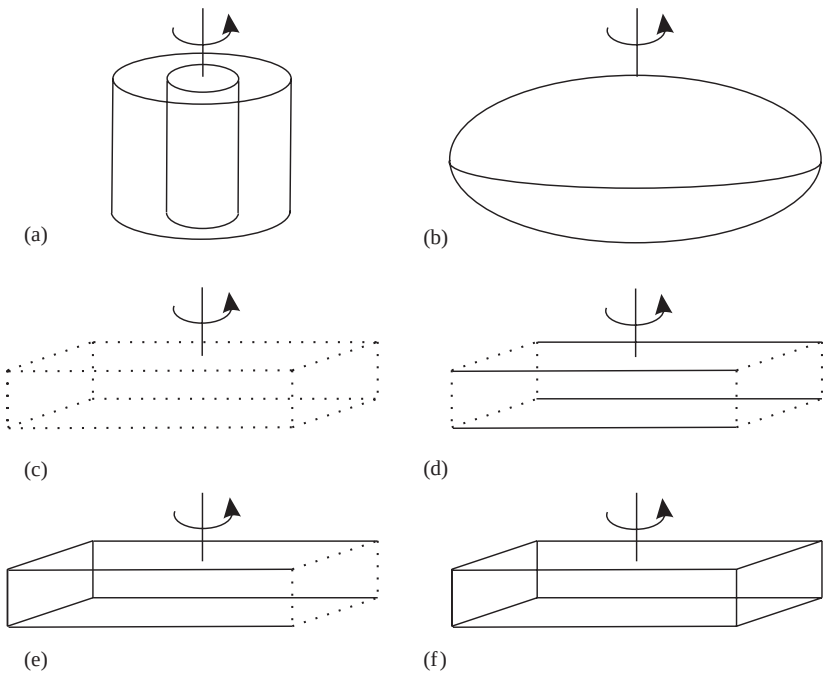

Fig. 1. Geometries for which inertial waves have been computed: (a) axial cylindrical can and (b) axial spheroid. Here inertial waves will be discussed in an infinite layer compressed between two parallel planes (c), in an infinite channel (d), a half-infinite channel (e) and in a box (f).

contrasts with surface gravity waves where this frequency can be compared to the eigenfrequency of the gravest, non-rotating mode of a rectangle (Rao, 1966). Also in distinction with surface waves increasing confinement does not lead to an isolated frequency spectrum, as one might naively expect. Inertial waves in a box have a dense frequency spectrum, which, moreover, is degenerate. In this respect, this is quite analogous to the case of (hydrostatic) *internal* gravity waves confined to a box in both non-rotating (see the appendix) and rotating stratified fluids (Bäuerle, 1998). However, while two-dimensional solutions of non-rotating internal gravity waves 'automatically' satisfy the impermeability conditions, because their rectilinear currents can be made parallel to vertical walls, this is no longer the case when the medium rotates and an intricate coupling of waves occurs, as illustrated by the confined inertial waves considered in this study. The adjustment of their circularly polarised currents to vertical side walls may therefore be more representative for the adjustment of gravito-inertial waves in 3D rotating containers, having elliptically polarised currents, and yet is simpler because of the absence of gravitational restoring.

Section 5 provides a discussion of the relevance of the results.

2. Governing equations

Small-amplitude waves in a homogeneous fluid that is rotating uniformly with angular frequency Ω_* about a vertical axis aligned in the z_* direction (asterisks denoting dimensional quantities) are

governed by the linearised, inviscid equations of motion on an f_*-plane (where $f_* = 2\Omega_*$):

$$\frac{\partial u_*}{\partial t_*} - f_* v_* = -\frac{1}{\rho_*}\frac{\partial p_*}{\partial x_*}, \tag{2.1}$$

$$\frac{\partial v_*}{\partial t_*} + f_* u_* = -\frac{1}{\rho_*}\frac{\partial p_*}{\partial y_*}, \tag{2.2}$$

$$\frac{\partial w_*}{\partial t_*} = -\frac{1}{\rho_*}\frac{\partial p_*}{\partial z_*}, \tag{2.3}$$

$$\frac{\partial u_*}{\partial x_*} + \frac{\partial v_*}{\partial y_*} + \frac{\partial w_*}{\partial z_*} = 0. \tag{2.4}$$

Here (u_*, v_*, w_*) are the velocity components in the three Cartesian directions (x_*, y_*, z_*), while ρ_* is the homogeneous density and p_* the reduced pressure (relative to the hydrostatic pressure).

In an infinite medium, the spatial structure of monochromatic waves $\propto \exp(-\mathrm{i}\sigma_* t_*)$ is thus governed by Poincaré's equation (Poincaré, 1885; Poincaré, 1910; Cartan, 1922; Greenspan, 1968)

$$\frac{\partial^2 p_*}{\partial x_*^2} + \frac{\partial^2 p_*}{\partial y_*^2} - \left(\frac{f_*^2}{\sigma_*^2} - 1\right)\frac{\partial^2 p_*}{\partial z_*^2} = 0, \tag{2.5}$$

obtained by combining (2.1)–(2.4). Plane waves $\propto \exp \mathrm{i}(\mathbf{k}_* \cdot \mathbf{x}_*)$, with $\mathbf{k}_* = (k_*, l_*, n_*)$, lead to the dispersion relation

$$\frac{\sigma_*}{f_*} = \pm\frac{n_*}{(k_*^2 + l_*^2 + n_*^2)^{1/2}} = \pm\sin\phi, \tag{2.6}$$

where ϕ is the angle which the wave vector makes with the plane perpendicular to the rotation axis. For frequencies $\sigma_* < f_*$, the hyperbolic nature of the Poincaré equation avoids the solution being boundary-trapped. Displacements will be largest in the interior of the fluid domain, resulting typically in a cellular wave pattern (Bjerknes et al., 1933). Plane waves propagate obliquely through the fluid, with an angle that is fixed with respect to the rotation axis (Görtler, 1944; Oser, 1958; McEwan, 1970). In the presence of a sloping boundary, this may therefore result in focusing of these waves, as observed experimentally (Maas, 2001; Manders and Maas, 2003).

Presently, we consider the container to have boundaries that respect the local reflectional symmetry of reflecting characteristics so that the walls are either exclusively parallel or perpendicular to the rotation axis. Starting with a flat, rigid bottom ($z_* = -H_*$) and surface ($z_* = 0$), perpendicular to the rotation axis, we require the vertical velocity to vanish there ($w_* = 0$ at $z_* = 0,\ -H_*$). The presence of the rigid surface removes the gravitational restoring force (and external gravity waves). Together, these boundaries enforce standing modes in the vertical and we make the dynamically consistent ansatz that the waves are given by

$$w_* = \sum_{n=1}^{\infty} \frac{\partial \zeta_{n*}}{\partial t_*} \sin\frac{n\pi z_*}{H_*}, \tag{2.7}$$

$$(u_*, v_*, p_*) = \sum_{n=1}^{\infty} (u_{n*}, v_{n*}, p_{n*}) \cos\frac{n\pi z_*}{H_*}. \tag{2.8}$$

Here subscript n refers to the nth vertical mode. This omits a steady, degenerate $n=0$ geostrophic mode, which has $w_{0*}=0$, $\rho_* f_* v_{0*} = \partial p_{0*}/\partial x_*$, $\rho_* f_* u_{0*} = -\partial p_{0*}/\partial y_*$, $\partial u_{0*}/\partial x_* + \partial v_{0*}/\partial y_* = 0$, for which the pressure field acts as a streamfunction, and which is not further considered here. The amplitude of the nth internal vertical elevation mode is denoted by ζ_{n*}. Substitution of these expansions in Eqs. (2.1)–(2.4) leads to

$$\frac{\partial u_{n*}}{\partial t_*} - f_* v_{n*} = -H_{n*} \frac{\partial^3 \zeta_{n*}}{\partial x_* \partial t_*^2}, \tag{2.9}$$

$$\frac{\partial v_{n*}}{\partial t_*} + f_* u_{n*} = -H_{n*} \frac{\partial^3 \zeta_{n*}}{\partial y_* \partial t_*^2}, \tag{2.10}$$

$$\frac{\partial \zeta_{n*}}{\partial t_*} + H_{n*} \left(\frac{\partial u_{n*}}{\partial x_*} + \frac{\partial v_{n*}}{\partial y_*} \right) = 0, \tag{2.11}$$

with effective depth

$$H_{n*} \equiv H_*/n\pi, \tag{2.12}$$

after eliminating the pressure amplitude, which, from (2.3), reads

$$p_{n*} = \rho_* H_{n*} \frac{\partial^2 \zeta_{n*}}{\partial t_*^2}. \tag{2.13}$$

Eqs. (2.9)–(2.11) are analogous to the familiar, linearised long wave equations (LWE), except that wave acceleration ($H_{n*}\partial_{t_* t_*}$) at the right-hand sides of Eqs. (2.9) and (2.10) replaces gravitational acceleration g_*, see LeBlond and Mysak (1978). The similarities and differences with the LWE will be further discussed in the next section.

3. Wave solutions

Picking just one particular mode, n, Eqs. (2.9)–(2.11) are non-dimensionalized by taking effective depth, H_{n*}, and inertial frequency f_* as length and frequency scales, respectively. Thus, writing $(u,v) = (u_{n*}, v_{n*})/H_{n*} f_*$, $\zeta = \zeta_{n*}/H_{n*}$, $t = t_* f_*$, $\sigma = \sigma_*/f_*$ and $(x,y) = (x_*, y_*)/H_{n*}$, the dimensionless equations, employing the subscript-derivative convention, become

$$u_t - v + \zeta_{ttx} = 0, \tag{3.1}$$

$$v_t + u + \zeta_{tty} = 0, \tag{3.2}$$

$$\zeta_t + u_x + v_y = 0. \tag{3.3}$$

By cross-differentiation of the momentum equations we obtain the polarization equations, relating velocity and elevation fields:

$$(\partial_{tt} + 1)u = -\partial_{tt}(\zeta_{tx} + \zeta_y), \tag{3.4}$$

$$(\partial_{tt} + 1)v = -\partial_{tt}(\zeta_{ty} - \zeta_x). \tag{3.5}$$

These equations, combined with (3.3), yield

$$[1 + (1 - \Delta)\partial_{tt}]\zeta_t = 0, \tag{3.6}$$

where Laplacian $\Delta = \partial_{xx} + \partial_{yy}$. The horizontal spatial structure of monochromatic waves $\propto \exp(-\mathrm{i}\sigma t)$ is thus determined by a Helmholtz equation

$$(\Delta + \kappa^2)(u, v, \zeta) = 0, \tag{3.7}$$

where

$$\kappa^2 = \frac{1}{\sigma^2} - 1 \tag{3.8}$$

and, for inertial waves, $\sigma < 1$. Horizontal velocities are now given by

$$u = \kappa^{-2}(-\mathrm{i}\sigma\zeta_x + \zeta_y), \tag{3.9}$$

$$v = \kappa^{-2}(-\mathrm{i}\sigma\zeta_y - \zeta_x). \tag{3.10}$$

At vertical walls these give rise to oblique-derivative boundary conditions, similar as for external long waves. A difference with the LWE is the definition of κ^2, Eq. (3.8), which, for external waves (scaled with the Rossby deformation radius, $(g_* H_*)^{1/2}/f_*$), reads $\sigma^2 - 1$, with $\sigma > 1$. Another difference is that the vertical mode number n of the inertial waves is hidden in the (dimensionless) size of the basin, so that a container of given size has a *double* infinite number of horizontal modes (one single infinite number for each vertical mode), while the external modes of the LWE have only a single infinite number of modes. The issue whether amongst the double infinite inertial modes there is a degeneracy (eigenfrequency multiplicity) will be addressed later on.

3.1. Plane inertial Poincaré waves

A vertically standing mode, (2.7) and (2.8), may propagate horizontally as a plane wave, of the form $\exp \mathrm{i}(kx + ly - \sigma t)$. Such a wave solves Eqs. (3.1)–(3.3) provided frequency and wave number satisfy the following dispersion relation (Tolstoy, 1973; Yamagata, 1978; Brekhovskikh and Goncharov, 1993):

$$\sigma = \frac{1}{(1 + k^2 + l^2)^{1/2}} = \frac{1}{(1 + \kappa^2)^{1/2}}, \tag{3.11}$$

where, by convention, we adopt positive frequencies only. Note that if we would have scaled the wave numbers just with H_*/π, instead of H_{n*}, a factor n (n^2) would show up in the numerator (denominator), in agreement with (2.6). From (3.8) the second identity is obtained, and identifies $\kappa = (k^2 + l^2)^{1/2}$ as the amplitude of the horizontal component of the wave number vector $\mathbf{k} = (k, l) \equiv \kappa(\cos\theta, \sin\theta)$. This dispersion relation shows the familiar property that inertial waves are low-frequency waves $\sigma < 1$ ($\sigma_* < f_*$). The fact that the frequency does not depend on the horizontal wave vector direction θ reveals the isotropy of the f-plane (invariance of (3.1)–(3.3) to rotation in horizontal plane). The phase velocity vector of the horizontally propagating wave is aligned with the group velocity vector in this plane. Their magnitudes are given by $c = \sigma/\kappa = \kappa^{-1}(1 + \kappa^2)^{-1/2}$ and $c_\mathrm{g} = \mathrm{d}\sigma/\mathrm{d}\kappa = -\kappa(1 + \kappa^2)^{-3/2}$, respectively, which shows that phase and energy propagate in opposite directions. The group velocity has an absolute maximum at $\kappa = 2^{-1/2}$, where $|c_\mathrm{g}| = 2/3^{3/2}$ (Fig. 2).

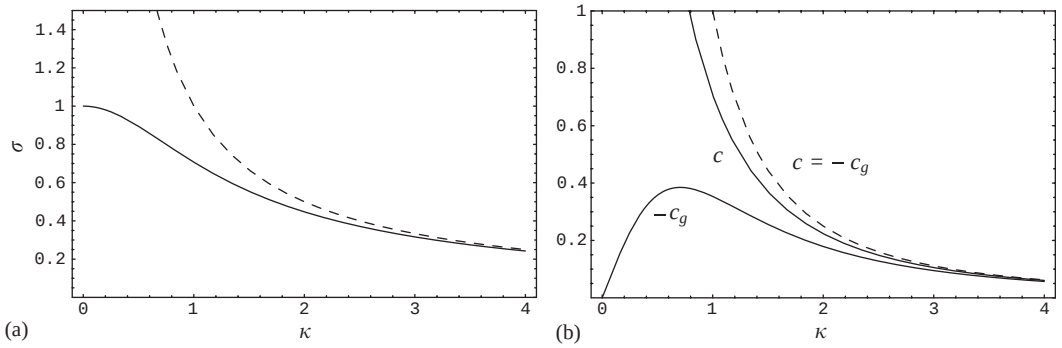

Fig. 2. (a) Dispersion relation of inertial Poincaré (solid) and inertial Kelvin (dashed) waves giving frequency versus wave number amplitude κ. (b) Corresponding phase velocity (c) and group velocity ($-c_g$) as a function of wave number amplitude. For IK waves, $c = -c_g$.

3.2. Inertial Kelvin wave

It is interesting to consider whether Eqs. (3.1)–(3.3) allow for inertial Kelvin (IK) waves, in the presence of a vertical wall, at $x = 0$, say. External Kelvin waves are semi-geostrophic, non-dispersive waves, having velocities parallel to the wall (LeBlond and Mysak, 1978). Searching for IK-solutions of Eqs. (3.1)–(3.3), we thus set $u = 0$. Consequently, these waves need to satisfy

$$-v = -\zeta_{ttx}, \tag{3.12}$$

$$v_t = -\zeta_{tty}, \tag{3.13}$$

$$\zeta_t + v_y = 0. \tag{3.14}$$

Combining the last two equations one finds

$$\partial_t(v - v_{yy}) = 0, \tag{3.15}$$

which, together with (3.12), shows that along-wall velocities v either grow or decay with along-wall distance y. From these equations it follows that a plane IK wave is a purely transversal wave (particle motion perpendicular to wave motion) of form

$$u = 0, \quad v = V\exp[-y + \mathrm{i}(x/\sigma - \sigma t)], \quad \zeta = \mathrm{i}\frac{v}{\sigma}, \tag{3.16}$$

provided it satisfies the dispersion relation

$$\sigma = 1/k. \tag{3.17}$$

Here V is an undetermined (complex) amplitude. As for the plane inertial waves, considered in the previous section, energy propagates ($c_g = -k^{-2}$) in a direction opposite to the phase ($c = k^{-2}$). IK waves thus decay in the direction of increasing y, while propagating their phase in the direction of increasing x (and vice versa, for waves growing with y). As the boundary at $x = 0$ is not employed at all (other than to impose the condition $u = 0$ in a natural way), in retrospect, this IK wave is more properly considered as being trapped to $y = 0$ and propagating in x (energy propagation in negative

x-direction). At the same time, however, such a wave cannot exist by itself, since it does not satisfy the impermeability condition ($v = 0$) at the latter boundary. Strictly speaking, therefore, *free* IK waves do not exist. In Section 3.4, we will show that Inertial Kelvin waves may, however, play a crucial role when inertial Poincaré (IP) waves reflect off a wall perpendicular to their propagation direction (at $y = 0$, say).

3.3. Inertial Poincaré waves in a channel

In the presence of a vertical wall at $x = 0$, plane IP waves exist when the velocity component perpendicular to that wall vanishes, $u = 0$. From the polarization equation (3.4), this requires

$$\zeta_{xt} + \zeta_y = 0 \quad \text{at } x = 0. \tag{3.18}$$

In the horizontal plane, inertial waves reflect specularly. Hence, a pair of incoming and reflected waves, that have identical frequency σ and along-wall wave number l,

$$\zeta = Z_i \exp \mathrm{i}(-kx + ly - \sigma t + \phi) + Z_r \exp \mathrm{i}(kx + ly - \sigma t - \phi), \tag{3.19}$$

needs to satisfy $-\sigma\zeta_x + l\zeta = 0$ at $x = 0$, or,

$$Z_i(\mathrm{i}k\sigma + l)\exp(\mathrm{i}\phi) + Z_r(-\mathrm{i}k\sigma + l)\exp(-\mathrm{i}\phi) = 0. \tag{3.20}$$

Hence, Z_i/Z_r equals the ratio of a quantity and its complex conjugate, and therefore equals a complex exponential, and the reflected wave thus has the same amplitude as the incident wave, $Z_r = Z_i \equiv Z/2$, suffering only a loss of phase ϕ. Perpendicular to the wall, the resulting wave is therefore of standing type

$$\zeta = Z\cos(kx - \phi)\exp \mathrm{i}(ly - \sigma t) = Z'\left(\cos kx + \frac{l}{\sigma k}\sin kx\right)\exp \mathrm{i}(ly - \sigma t), \tag{3.21}$$

provided $\exp(-2\mathrm{i}\phi) = (k\sigma - \mathrm{i}l)/(k\sigma + \mathrm{i}l)$, or $\phi = \tan^{-1}(l/k\sigma)$, so that $\tan\theta = \sigma\tan\phi$, where, recall, θ is the direction of the wave number vector in the horizontal plane with respect to the cross-channel (x) direction. With the latter expression for ζ (and a transformed amplitude $Z' = Z\cos\phi$), from (3.9), the velocity component perpendicular to the wall becomes

$$u = \mathrm{i}kZ'\frac{\sigma^3}{1 - \sigma^2}\left(1 + \left(\frac{l}{\sigma k}\right)^2\right)\sin kx \exp \mathrm{i}(ly - \sigma t), \tag{3.22}$$

so that IP waves can exist also in a channel of (non-dimensional) width L when cross-channel wave numbers are quantized:

$$k \in \left\{k_m = \frac{m\pi}{L}\right\}, \quad m \in \{1, 2, 3, \ldots\}. \tag{3.23}$$

The along-channel velocity component of the combined IP waves is, from (3.10),

$$v = Z'\left(-l\sigma\cos kx + \frac{1}{k}\sin kx\right)\exp \mathrm{i}(ly - \sigma t). \tag{3.24}$$

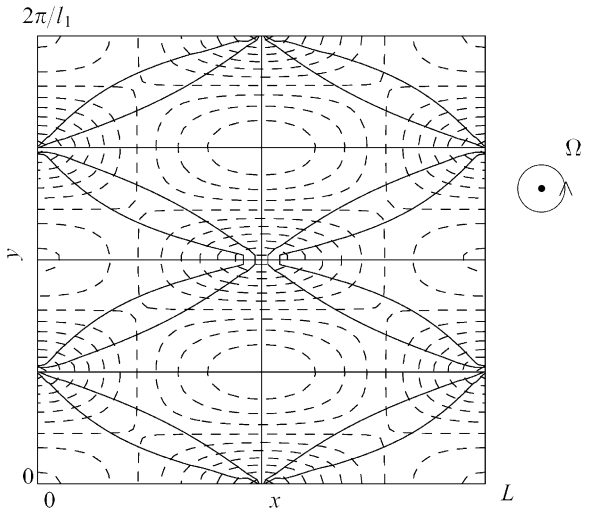

Fig. 3. Top view of one wave length segment of a channel which is infinitely long in y-direction and of dimensionless width $L = 4$ in x-direction. It shows phase (solid) and amplitude (dashed lines) of the vertical displacement field of a pair of equal amplitude, mode-1, up and down channel propagating Poincaré modes of frequency $\sigma = 0.7$. Amplitudes are maximum at the saddle nodes of phase lines, located on the channel axis, at 1/4 and 3/4 wavelength. Rotation axis, designated by $\mathbf{\Omega}$, points out of the paper.

The phase lines $ly - \sigma t = \text{const.}$ propagate in positive y-direction (energy in negative y-direction). At fixed instance t, any single channel mode will have phase line $y = \text{const.}$, which is perpendicular to the channel walls. Because of the asymmetry caused by Coriolis forces this is no longer true for a combination of up and down-channel propagating inertial Poincaré waves, such as shown for two of equal magnitude in Fig. 3. It displays the typical amphidromic nature of the combined wave system, characterized by phase lines circling anticyclonically (i.e. clockwise) around nodal points where vertical elevation vanishes, similar to the well-known phase pattern displayed by counterpropagating (external) Kelvin (LeBlond and Mysak, 1978) or Poincaré waves (Krauss, 1973; Mortimer, 1974; Hutter, 1993). Such phase pattern was first conjectured long ago by (Whewell, 1833) to comprehensively describe observed tidal elevation patterns, see (Cartwright, 1999). Amphidromic patterns were recently recognized to occur also in the vertical plane, in 2D obliquely propagating internal waves (deWitt et al., 1986; Gerkema, 2001), and in quantum mechanical wave systems (Berry, 1987).

3.4. Inertial Poincaré channel waves reflecting from a vertical wall

Rewrite the general dispersion relation, (2.6), replacing k by k_m, Eq. (3.23). Then, the along-channel wave number is determined by

$$l_m = \pm(\sigma^{-2} - 1 - k_m^2)^{1/2} \equiv \pm(\sigma^{-2} - \sigma_m^{-2})^{1/2}, \tag{3.25}$$

where the cut-off frequency is

$$\sigma_m = (1 + k_m^2)^{-1/2} < 1. \tag{3.26}$$

For any given σ and m, these IP channel waves share the property with the external Poincaré channel waves that they are restricted in frequency space. In this case they can exist as propagating waves ($l_m^2 > 0$) only if their frequency is less then the cut-off frequency σ_m. Notice that frequencies may equal these bounding frequencies, σ_m, and then represent waves that are uniform in along-channel direction ($l = 0$), which are standing in the cross-channel plane. All propagating IP waves, though, are bounded from above by σ_1. For any given frequency $\sigma < \sigma_1$, the higher cross-channel modes ($m \in \{M, M+1, \ldots\}$) will always be trapped, where M is the smallest m for which $\sigma_m < \sigma$. This is relevant for the case that an incoming Poincaré wave, whose energy propagates along the negative y-direction ($l_m > 0$), reflects from a perpendicular wall at $y = 0$. Apart from the directly reflected wave of the same, but oppositely signed wave number, discussed in the previous paragraph, some of its energy may be scattered into the IK and higher mode IP waves. The IK wave is always evanescent, but the other IP waves will be evanescent only when the incoming wave is a fundamental mode ($m = 1$) of frequency σ that lies in the interval, $\sigma_2 < \sigma < \sigma_1 < 1$. If $\sigma < \sigma_2$, however, some energy may leak to lower-mode, propagating channel IP waves. The reflection problem is similar to that considered by (Taylor, 1921), concerned with Kelvin wave reflection at the dead end of a tidal channel, except that the incoming wave here necessarily has to be of the above IP type.

Let us consider the reflection at $y = 0$ of an $m = 1$ wave coming from positive y. The total along-channel velocity is then composed of an incoming wave (of unit amplitude) of the form (3.24) having along-channel wave number $+l_1$, a trapped IK wave, see (3.16), and an infinite sum of 'reflected' IP waves, again of the form (3.24) but with negative sign of along-channel wave number. Dropping a common factor $\exp(-\mathrm{i}\sigma t)$, these three contributions read

$$v = \left(-l_1\sigma\cos k_1 x + \frac{1}{k_1}\sin k_1 x\right)\exp(\mathrm{i}l_1 y) + v_0\exp(-y + \mathrm{i}x/\sigma) + \sum_{m=1}^{\infty} v_m\left(l_m\sigma\cos k_m x + \frac{1}{k_m}\sin k_m x\right)\exp(-\mathrm{i}l_m y), \tag{3.27}$$

where the amplitudes of the IK wave (v_0) and the reflected IP waves ($v_{1,2,\ldots}$) need to be determined by the condition $v = 0$ at $y = 0$. Since the IP modes with mode number $m > 1$ are all trapped, we set in that case

$$l_m = -\mathrm{i}(\sigma_m^{-2} - \sigma^{-2})^{1/2} \equiv -\mathrm{i}s_m \quad (s_m > 1). \tag{3.28}$$

The undetermined wave amplitudes are estimated by means of the collocation method (see LeBlond and Mysak, 1978). In this method the infinite sum is truncated to include just $M-1$ channel modes. Evaluating the boundary condition at M x-positions along the wall, yields M equations, from which the M unknown (complex) amplitudes $v_0 \ldots v_{M-1}$ can be obtained by matrix inversion. Convergence of the solution has to be checked a posteriori. Following this recipe, the solution in Fig. 4 is obtained with $M = 21$. Fig. 4a shows the amplitude and phase of the vertical displacement field ζ. Phase propagates in clockwise direction, so that we infer that energy propagates anticlockwise. The response yields a complex amplitude $v_1 = \exp \mathrm{i}\phi_1$, which, correctly, is of unit magnitude, expressing that there is no leakage to other modes that propagate energy out of the channel. The phase-delay ϕ_1 of the reflected wave, corresponds to the fact that some of the energy is stored in the boundary waves at the end wall that help maintain the impermeability condition at $y = 0$. Both the IK,

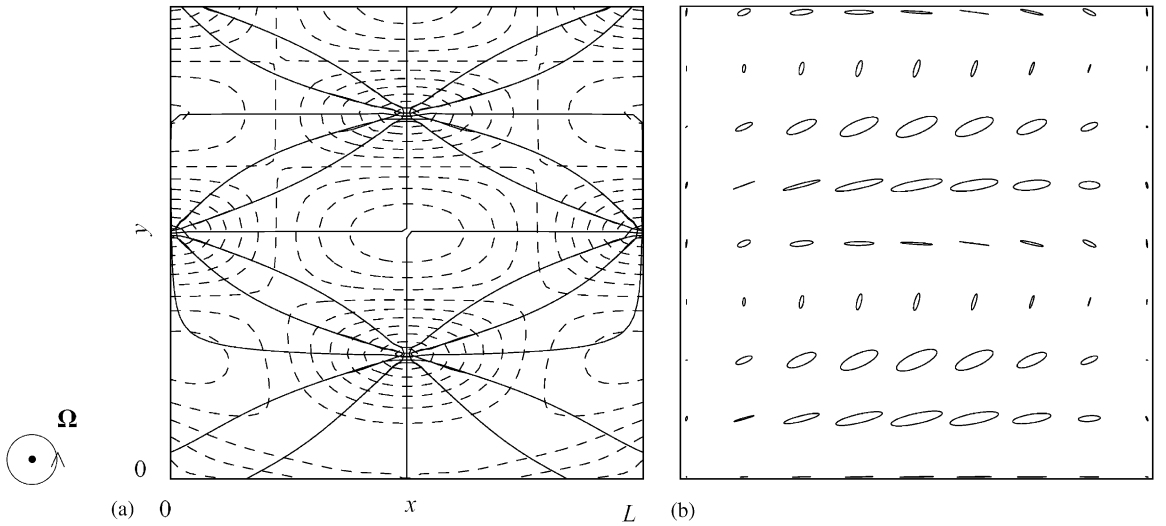

Fig. 4. Top view of: (a) phase (solid) and amplitude (dashed) of the vertical displacement field of a mode-1, down-channel propagating Inertial Poincaré mode of frequency $\sigma = 0.7$ in a channel of dimensionless width $L = 4$, reflecting from a vertical wall at $y = 0$. During reflection, IK and IP waves are excited, that are trapped in the y-direction. Phase lines are given every 30°, which rotate anticyclonically around the amphidromes at the central axis (the rotation axis, $\mathbf{\Omega}$, is out of the paper); (b) horizontal current ellipses traversed during one period.

as well as the $m = 2, 3$ trapped IP waves have fairly strong amplitudes. Fig. 4b shows corresponding horizontal velocity ellipses at a number of positions. These are traversed clockwise, and their normal components correctly vanish at the boundaries.

4. Inertial waves in a rectangular parallelepiped

In this section a solution is sought for the nth vertical mode in a rectangular parallelepiped. We will use the Proudman–Rao spectral method (Proudman, 1916; Rao, 1966), designed for rotationally modified surface gravity waves in regions of arbitrary cross-section, and here altered for our purpose to the study of pure inertial waves. We will closely follow Rao's application to a rectangular domain, for which geometry the method was, for the case of surface gravity waves, first checked to compare favourably up to at least 3 digits with results obtained by a completely different method (Taylor, 1921), not further discussed here.

4.1. The Proudman–Rao spectral method

The method employs a Helmholtz decomposition of the velocity field, whose velocity potential and streamfunction fields can be expanded in the eigenfunctions of two eigenvalue problems. The time-dependent expansion coefficients are dynamically coupled in a way that can probably be calculated explicitly for simply-shaped containers only. Proudman (1916) did this for the axial cylinder, of both uniform and paraboloidal depth shape, and retrieved results as listed in an earlier edition of

Lamb (1932). Rao (1966) used the method to retrieve and extend Taylor's results for rotationally modified gravity waves in the rectangle (Taylor, 1921). Here we will briefly describe the method as applied to pure inertial waves in a rectangular parallelepiped.

Aiming to solve (3.1)–(3.3), the horizontal velocity field $\mathbf{v} = (u, v)$ is split in an irrotational ($\mathbf{v}^{\phi} = -\boldsymbol{\nabla}\phi$) and a non-divergent ($\mathbf{v}^{\psi} = \hat{\mathbf{k}} \times \nabla\psi$) part (Helmholtz decomposition):

$$\mathbf{v} = \mathbf{v}^{\phi} + \mathbf{v}^{\psi}. \tag{4.1}$$

Here $\hat{\mathbf{k}}$ is a (vertical) unit vector, aligned with the rotation axis. The impermeability requirement at the boundary, $\mathbf{v} \cdot \mathbf{n} = 0$, where $\mathbf{n}$ denotes the outward-directed normal, translates into a requirement that $\partial\phi/\partial n = 0$ and $\psi = 0$ at the boundary. The velocity potential ϕ, streamfunction ψ and vertical elevation field ζ are represented as

$$\phi = \sum_{\alpha} p_{\alpha}\phi_{\alpha}, \tag{4.2}$$

$$\psi = \sum_{\alpha} q_{\alpha}\psi_{\alpha}, \tag{4.3}$$

$$\zeta = \sum_{\alpha} r_{\alpha}\zeta_{\alpha}, \tag{4.4}$$

where $\alpha \equiv (k, l)$ represents a (binary) ordering index, indicating a pair of (generalized Fourier) modes, with mode numbers k and l (zero or positive integers) in x and y direction, respectively. Notice that each normal mode (eigenfunction corresponding to a particular eigenfrequency) thus consists of an infinite sum of such Fourier modes. Expansion coefficients p_{α}, q_{α}, r_{α} are time-dependent, while ϕ_{α} and ψ_{α} are internally orthogonal (real) spectral spatial functions. The latter are determined as the solutions of two elliptic operators (as (3.7), but with simpler boundary conditions)

$$\Delta\phi_{\alpha} + \lambda_{\alpha}\phi_{\alpha} = 0, \quad \frac{\partial\phi_{\alpha}}{\partial n} = 0 \quad \text{at boundary}, \tag{4.5}$$

$$\Delta\psi_{\alpha} + \mu_{\alpha}\psi_{\alpha} = 0, \quad \psi_{\alpha} = 0 \quad \text{at boundary}. \tag{4.6}$$

Self-adjointness of these operators implies that λ_{α} and μ_{α} are real. From the continuity equation (3.3), it follows that

$$\zeta_{\alpha} = \lambda_{\alpha}^{1/2}\phi_{\alpha}. \tag{4.7}$$

Defining consistently

$$\mathbf{v}_{\alpha}^{\phi} = -\boldsymbol{\nabla}\phi_{\alpha}, \tag{4.8}$$

$$\mathbf{v}_{\alpha}^{\psi} = \hat{\mathbf{k}} \times \boldsymbol{\nabla}\psi_{\alpha}, \tag{4.9}$$

orthogonality of these functions can be established, employing partial integration and use of boundary conditions:

$$\int \mathbf{v}_{\alpha}^{\phi} \cdot \mathbf{v}_{\beta}^{\phi}\, \mathrm{d}A = \lambda_{\alpha} \int \phi_{\alpha}\phi_{\beta}\, \mathrm{d}A = \delta_{\alpha\beta}A, \tag{4.10}$$

$$\int \mathbf{v}_\alpha^\psi \cdot \mathbf{v}_\beta^\psi \,\mathrm{d}A = \mu_\alpha \int \psi_\alpha \psi_\beta \,\mathrm{d}A = \delta_{\alpha\beta} A. \tag{4.11}$$

Here A represents the horizontal cross-sectional area. Also

$$\int \zeta_\alpha \zeta_\beta \,\mathrm{d}A = (\lambda_\alpha \lambda_\beta)^{1/2} \int \phi_\alpha \phi_\beta \,\mathrm{d}A = \delta_{\alpha\beta} A. \tag{4.12}$$

Using this, the expansion coefficients can be defined as projections of the velocity field on these functions:

$$p_\alpha \equiv \frac{1}{A} \int \mathbf{v}_\alpha^\phi \cdot \mathbf{v}^\phi \,\mathrm{d}A = \frac{1}{A} \int \mathbf{v}_\alpha^\phi \cdot \mathbf{v} \,\mathrm{d}A, \tag{4.13}$$

$$q_\alpha \equiv \frac{1}{A} \int \mathbf{v}_\alpha^\psi \cdot \mathbf{v}^\psi \,\mathrm{d}A = \frac{1}{A} \int \mathbf{v}_\alpha^\psi \cdot \mathbf{v} \,\mathrm{d}A, \tag{4.14}$$

$$r_\alpha \equiv \frac{1}{A} \int \zeta_\alpha \zeta \,\mathrm{d}A. \tag{4.15}$$

By inserting the expansions of the velocity and elevation fields in Eqs. (3.1)–(3.3), multiplying these equations by the orthogonal spatial functions and by subsequently integrating over the spatial domain, evolution equations for the spectral expansion coefficients result. Coupling of modes is due to the non-vanishing of the following integrals:

$$a_{\alpha\beta} = -\frac{1}{A} \int \mathbf{v}_\alpha^\phi \cdot \hat{\mathbf{k}} \times \mathbf{v}_\beta^\phi \,\mathrm{d}A, \tag{4.16}$$

$$b_{\alpha\beta} = -\frac{1}{A} \int \mathbf{v}_\alpha^\phi \cdot \hat{\mathbf{k}} \times \mathbf{v}_\beta^\psi \,\mathrm{d}A, \tag{4.17}$$

$$c_{\alpha\beta} = -\frac{1}{A} \int \mathbf{v}_\alpha^\psi \cdot \hat{\mathbf{k}} \times \mathbf{v}_\beta^\phi \,\mathrm{d}A. \tag{4.18}$$

Thus, the following equations result:

$$\frac{\mathrm{d}p_\alpha}{\mathrm{d}t} = v_\alpha \frac{\mathrm{d}^2 r_\alpha}{\mathrm{d}t^2} + \sum_\beta (a_{\alpha\beta} p_\beta + b_{\alpha\beta} q_\beta), \tag{4.19}$$

$$\frac{\mathrm{d}q_\alpha}{\mathrm{d}t} = \sum_\beta c_{\alpha\beta} p_\beta, \tag{4.20}$$

$$\frac{\mathrm{d}r_\alpha}{\mathrm{d}t} = -v_\alpha p_\alpha, \tag{4.21}$$

where $v_\alpha = \lambda_\alpha^{1/2}$. For the rectangular domain ($0 \leqslant x \leqslant L_x$, $0 \leqslant y \leqslant L_y$) the solutions of (4.5) and (4.6) are

$$\phi_\alpha = \varepsilon_\alpha v_\alpha^{-1} \cos(k\pi x/L_x) \cos(l\pi y/L_y) \tag{4.22}$$

and

$$\psi_\alpha = 2 v_\alpha^{-1} \sin(k\pi x/L_x) \sin(l\pi y/L_y), \tag{4.23}$$

where

$$\mu_\alpha = \lambda_\alpha = \nu_\alpha^2 = \pi^2 \left(\frac{k^2}{L_x^2} + \frac{l^2}{L_y^2} \right) \tag{4.24}$$

and Neumann symbol ε_α equals $2^{1/2}$ when $kl = 0$, and 2 otherwise. Taylor (1921) found that normal modes are either symmetric (so that arbitrary $F(x, y) = F(L_x - x, L_y - y)$) or antisymmetric ($F(x, y) = -F(L_x - x, L_y - y)$). This was asserted by Rao (1966) by noting that $a_{\alpha\beta}$ vanishes if α and β have opposite symmetry (the symmetry or antisymmetry of the characteristic functions ϕ_α, ψ_α being determined by $k + l$ being even, or odd). Note that 'symmetric' fields here refer to a *point* symmetry of the velocity potential, streamfunction and vertical elevation field with respect to the centre of the basin, to which correspond *antisymmetric* velocity fields, by Eqs. (4.8) and (4.9) (and vice versa). Therefore, Rao (1966) distinguishes the following two cases: antisymmetric modes, for which $k + l$ is odd, which is achieved by either $\alpha \equiv (k, l)$, having k odd and l even, or $\alpha' \equiv (k', l')$, having k' even and l' odd; and symmetric modes, for which $k + l$ is even, achieved by either $\alpha \equiv (k, l)$, having k odd and l odd, or $\alpha' \equiv (k', l')$, having k' even and l' even. Again, as Rao (1966) notes, coupling vanishes if both modes belong to the same α group, or to the same α' group. These two groups have a different reflectional, or *line* symmetry. Here $F(x, y)$ is said to be x-symmetric (+) or x-antisymmetric (−) when $F(L_x - x, y) = \pm F(x, y)$. With a similar definition for y-(anti)symmetry, ϕ_α and $\psi_{\alpha'}$ have x-antisymmetry and y-symmetry, while $\phi_{\alpha'}$ and ψ_α have x-symmetry and y-antisymmetry. With this distinction, separate evolution equations for α and α' modes need to be distinguished and leads, in comprehensive notation, to

$$\mathrm{d}\mathbf{p}/\mathrm{d}t = \mathbf{N}\mathrm{d}^2\mathbf{r}/\mathrm{d}t^2 + (\mathbf{A}\mathbf{p}' + \mathbf{B}\mathbf{q}'), \quad \mathrm{d}\mathbf{q}/\mathrm{d}t = \mathbf{C}\mathbf{p}', \quad \mathrm{d}\mathbf{r}/\mathrm{d}t = -\mathbf{N}\mathbf{p}, \tag{4.25}$$

$$\mathrm{d}\mathbf{p}'/\mathrm{d}t = \mathbf{N}'\mathrm{d}^2\mathbf{r}'/\mathrm{d}t^2 - (\mathbf{A}^{\mathrm{T}}\mathbf{p} + \mathbf{C}^{\mathrm{T}}\mathbf{q}), \quad \mathrm{d}\mathbf{q}'/\mathrm{d}t = -\mathbf{B}^{\mathrm{T}}\mathbf{p}, \quad \mathrm{d}\mathbf{r}'/\mathrm{d}t = -\mathbf{N}'\mathbf{p}'. \tag{4.26}$$

Here superscript T denotes a transpose, and a vector like $\mathbf{p}$ denotes the column-vector $p_i \equiv p_{\alpha_i}$. Integer i refers to a specific ordering of the α, that is, of the subclass on the (k, l) lattice associated with this symmetry. In the same vein, a matrix like $\mathbf{A} = a_{ij} = a_{\alpha_i \alpha'_j}$, while $\mathbf{N} = \nu_{\alpha_i}\delta_{ij}$ denotes the diagonal matrix.

For the rectangle, the matrix coefficients reduce to (Rao, 1966)

$$a_{\alpha\alpha'} = \frac{4\varepsilon_\alpha \varepsilon_{\alpha'}(k'^2 l^2 - k^2 l'^2)}{L_x L_y \nu_\alpha \nu_{\alpha'}(k^2 - k'^2)(l^2 - l'^2)}, \tag{4.27}$$

$$b_{\alpha\alpha'} = \frac{-8\varepsilon_\alpha \nu_\alpha k' l'}{\pi^2 \nu_{\alpha'}(k^2 - k'^2)(l^2 - l'^2)}, \tag{4.28}$$

$$c_{\alpha\alpha'} = \frac{8\varepsilon_{\alpha'} \nu_{\alpha'} kl}{\pi^2 \nu_\alpha (k^2 - k'^2)(l^2 - l'^2)}. \tag{4.29}$$

Inserting the ansatz

$$(\mathbf{p}, \mathbf{q}, \mathbf{r}') = (\mathbf{P}, \mathbf{Q}, \mathbf{R}') \sin \sigma t, \tag{4.30}$$

$$(\mathbf{p}', \mathbf{q}', \mathbf{r}) = (\mathbf{P}', \mathbf{Q}', \mathbf{R}) \cos \sigma t, \tag{4.31}$$

into the spectral equations, leads upon elimination of

$$(\mathbf{Q},\mathbf{Q}',\mathbf{R},\mathbf{R}') = \frac{1}{\sigma}(\mathbf{CP}',\mathbf{B}'\mathbf{P},\mathbf{NP},-\mathbf{N}'\mathbf{P}') \tag{4.32}$$

to the following equations:

$$(\sigma^2(\mathbf{I}+\mathbf{N}^2)-\mathbf{BB}^{\mathrm{T}})\mathbf{P}-\sigma\mathbf{AP}'=0, \tag{4.33}$$

$$-\sigma\mathbf{A}^{\mathrm{T}}\mathbf{P}+(\sigma^2(\mathbf{I}+\mathbf{N}'^2)-\mathbf{C}^{\mathrm{T}}\mathbf{C})\mathbf{P}'=0, \tag{4.34}$$

where $\mathbf{I}$ is the identity matrix and σ the undetermined normal mode frequency. Non-trivial solutions occur when the determinant of the matrix multiplying the columnvector $\mathbf{X}=(\mathbf{P},\mathbf{P}')$ vanishes. Because of the quadratic appearance of eigenfrequency σ, this classifies as a quadratic eigenvalue problem. Abbreviating Eqs. (4.33) and (4.34) as

$$(\sigma^2\mathbf{M}_2+\sigma\mathbf{M}_1+\mathbf{M}_0)\mathbf{X}=0 \tag{4.35}$$

with obvious meanings of matrices $\mathbf{M}_{0,1,2}$, this can be rewritten as a 'normal' generalized eigenvalue problem (Bai et al., 2000)

$$\mathscr{A}\mathbf{Y}=\sigma\mathscr{B}\mathbf{Y}, \tag{4.36}$$

where

$$\mathscr{A}=\begin{bmatrix}\mathbf{0} & \mathbf{I}\\ -\mathbf{M}_0 & -\mathbf{M}_1\end{bmatrix},\quad \mathscr{B}=\begin{bmatrix}\mathbf{I} & \mathbf{0}\\ \mathbf{0} & \mathbf{M}_2\end{bmatrix} \tag{4.37}$$

and columnvector $\mathbf{Y}=(\mathbf{X},\sigma\mathbf{X})$, which can be solved with a general purpose eigenvalue solver (as Matlab's). After checking the code, by applying it to the LWE, and comparing with published eigenfrequencies (Taylor, 1921; Rao, 1966), it was used for the determination of eigenfrequencies and corresponding eigenvectors of inertial waves in a rectangular parallelepiped. Some results are discussed in the next section.

4.2. Numerical results

4.2.1. Mode truncation

In order to obtain numerical results, the infinite system of equations has to be truncated. Convergence of eigenvalues was observed by increasing the amount of Fourier modes I taken into account. Here $\alpha_i=(k_i,l_i)$, with $i=1,2,\ldots,I$ etc. The total number I depends on the amount of 'lattice lines', $N+1$, incorporated. The jth point ($0\leqslant j\leqslant n$) on the nth lattice line ($0\leqslant n\leqslant N$) defines the integer pairs $\alpha_i=(k_i,l_i)$ or $\alpha_i'=(k_i',l_i')$ of the ith ($i=n(n+1)/2+j+1$) Fourier mode included. As we will truncate while incorporating a number of full lattice lines, so that $j=n=N$, the total amount of Fourier modes taken into account is $I=(N/2+1)(N+1)$. For antisymmetric modes the prescription reads $k_i=l_i'=2(n-j)+1$, $l_i=k_i'=2j$, so that $k_i+l_i=k_i'+l_i'=2n+1$ are both odd. For symmetric modes $k_i=2(n-j)+1$, $l_i=2j+1$, and $k_i'=2j$, $l_i'=2(n-j)$, so that $k_i+l_i=2(n+1)$ and $k_i'+l_i'=2n$ are both even. Index value $n=0$ refers to the first lattice 'line', which consists of just one point. (Note that this convention implies that in the symmetric case $k_1'=l_1'=0$, in other words, that the corresponding fields are spatially constant. We will require the matrix coefficients belonging to this

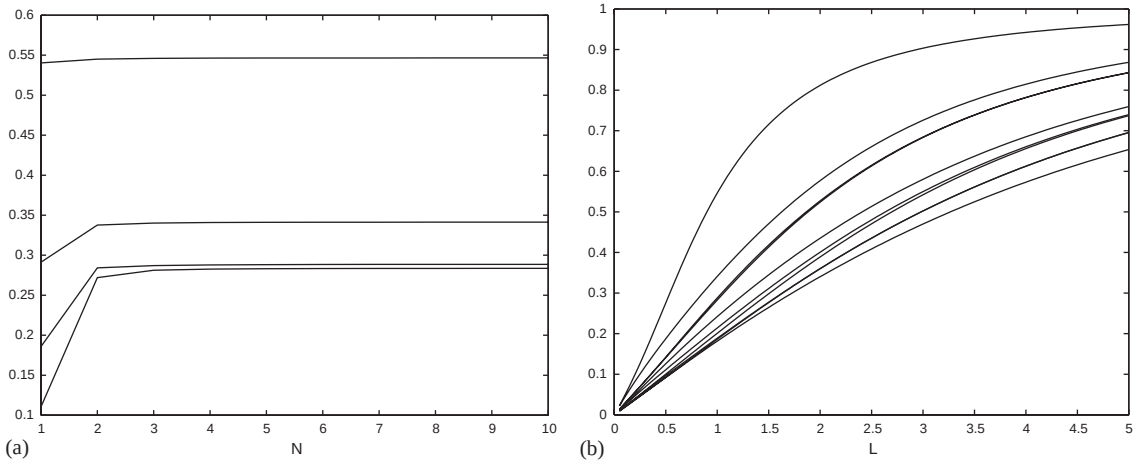

Fig. 5. (a) Convergence of first four eigenvalues corresponding to the asymmetric modes of a $\pi \times \pi$ square, as a function of the number of lattice lines N. (b) Same eigenvalues as a function of the (dimensionless) size of a square basin, L divided by π.

term to vanish identically, $a_{11} = b_{11} = c_{11} = 0$. This point is formally incorporated in the summations to facilitate a symmetric treatment between primed and unprimed modes.)

There are two dimensionless (geometric) parameters left in the problem, the width L_x and length L_y, or, alternatively, the size $L = (L_x^2 + L_y^2)^{1/2}$ and aspect ratio L_y/L_x. Added to this is a truncation parameter N which, according to the scheme layed out above, determines the amount of spatial modes I taken into account. We aim at choosing an N such that computations do not turn unwieldy, yet are sufficiently accurate. For a number of choices of geometric parameters, convergence of eigenvalues was established to occur to within 5 decimal places at $N = 12$, corresponding to $I = 91$ Fourier modes for each normal mode of fixed frequency (see Fig. 5a). This value was used for subsequent calculations. With the corresponding approximate velocity and elevation fields, numerical versions of the left-hand sides of Eqs. (3.1) and (3.2) can be computed. Because of numerical errors these residual fields differ from 0 (and show Gibb's phenomenon close to the boundary). The 2-norm of the computed residual field amounts typically to 5 percent of the norm of a typical term on the left-hand side.

4.2.2. *Eigenfrequencies*

Increasing the size of the basin L leads to a monotonic increase of eigenfrequencies, until for large basins these crowd just below the inertial frequency 1 (dimensionally: $2\Omega_*$), see Fig. 5b.

The plot of eigenfrequencies versus aspect ratio (Fig. 6) shows several remarkable features. Asymptotically ($L_y/L_x \gg 1$), from the highest frequency downward, it reveals an alternation of anti-symmetric (solid) and symmetric modes (dashed lines). The (anti) symmetry refers to that of the elevation field ζ. Moreover, despite the fact that eigenfrequencies in general change with changing aspect ratio, following a particular mode (line), there are certain fixed frequencies that continue to play a role as eigenfrequency, albeit shifting from one spatial mode to the next. These are the plateaus, the horizontal lines at $\sigma = \sigma_m$, $m = 1, 2, 3, \ldots$, several of which can be recognized in Fig. 6.

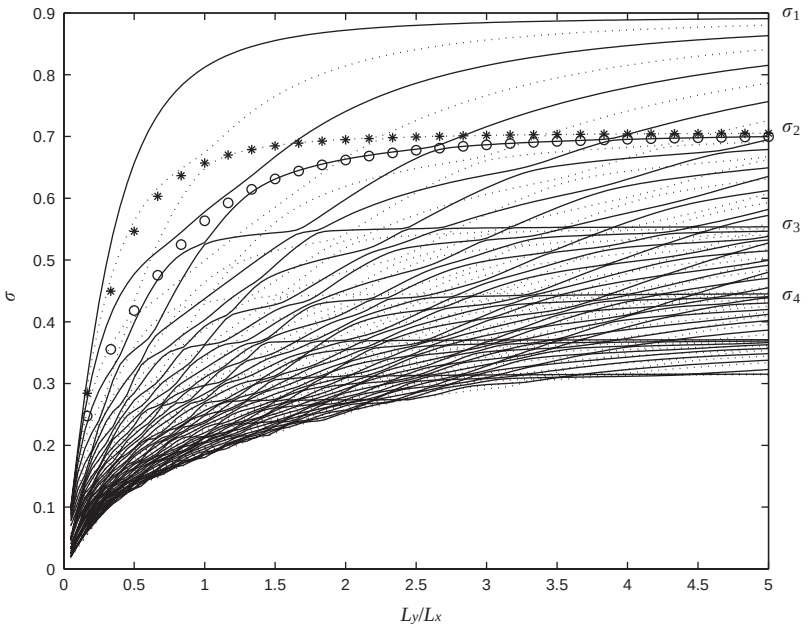

Fig. 6. Eigenvalues of first 50 modes as a function of aspect ratio, L_y/L_x for $L_x = 2\pi$. From the highest frequency down, these alternatingly depict the asymmetric (solid) and symmetric (dashed) elevation modes. Stars and circles, and frequencies $\sigma_{1,2,3,4}$, are discussed in the text.

This is remarkable, as, for very elongated containers, these truly act as natural frequencies, being independent of the exact aspect ratio. The values of these natural frequencies are, surprisingly, given by Eq. (3.26), which for $L_x = 2\pi$ read $\sigma_m = (1 + (m/2)^2)^{-1/2}$, $m \in \{1, 2, 3, 4, \ldots\}$. These are the frequencies corresponding to modes that are 'structureless' (have vanishing wave number) in the container's longest direction. As variation of frequency with varying aspect ratio can also be interpreted as a variation with varying (available) wave length, the occurrence of frequency plateaus also implies zero group velocity of that mode, in line with the idea that the mode is standing.

Solid curves (corresponding to antisymmetric modes) never cross each other. Neither do dashed curves (symmetric modes). Only neighbouring solid and dashed curves may cross, leading at intersection points to an unambiguous degeneracy of the eigenfrequency. This pattern is also displayed in eigenfrequency curves of long, rotationally modified internal gravity waves contained in a rectangular basin (Bäuerle, 1998).

In the discussion of the available parameters, that of the vertical mode number n was suppressed. It is present in the depth $H_n = H/n\pi$ with which width L_x and length L_y were scaled, and which was held fixed until now. However, a true basin only has its geometric parameters fixed, and we thus need to consider the effect of changing n. A change in n only affects the size and not the aspect ratio. If, for instance, we change from mode $n = 1$ to mode $n = 2$, the apparent width and length are both doubled. As Rao (1966) remarks, matrices $\mathbf{A}, \mathbf{B}$ and $\mathbf{C}$, Eqs. (4.27)–(4.29), depend only on the aspect ratio, and are hence not affected by this change in vertical mode number. In contrast, matrices $\mathbf{N}$ and $\mathbf{N}'$ are affected, so that it is a priori not clear whether there will be a degeneracy (multiplicity)

of eigenfrequencies, as in the 2D case (Maas and Lam, 1995), or as for internal gravity waves in the 3D case (see the appendix). The presence of this degeneracy allowed, in this 2D case, for a dual picture of these waves. These could either be considered as a set of vertically standing modes, or as an internal wave beam (Maas and Lam, 1995; Gerkema, 2001). Also, it led, in the 2D case, to the notion of a fundamental interval on the bounding surface, over which an arbitrarily chosen pressure field specified the otherwise non-unique solution. Whether multiplicity of eigenfrequencies still exists in the present 3D case, and whether the generalisation of the 2D interval, namely a fundamental *area*, can presently be found is not known. However, it is worthwhile to note that we can interpret the curves in Fig. 6 also as those belonging to the second vertical mode ($n = 2$) of a container of length, width and depth: $\pi \times L_y/2 \times H$. The first antisymmetric mode of the first vertical mode ($n = 1$) of such a container, is given by the line traced by the circles (asymptote at $\sigma_2 = 2^{-1/2}$). This mode is seen to partially overlap with successive $n = 2$ modes (solid lines), implying (near) degeneracy of the eigenfrequency. The line traced out by stars is the first antisymmetric ($n = 1$) eigenfrequency curves of a container measuring $2\pi \times L_y/2 \times H$, so that two of these containers fit in, side by side, in the original container, as seen from the perspective of the second vertical mode. Clearly, these curves again partially overlap with those of the second vertical mode (dashed lines), implying near-degeneracy.

4.2.3. Elevation and velocity fields

When a vertical mode is picked, $n = 1$ say, and the basin is scaled with the corresponding vertical scale, the eigenfrequencies are determined, and the corresponding elevation amplitude and velocity fields can be plotted. [Note that the actual vertical elevation is depth dependent, due to the vertical mode dependence, as in (2.7).] Counting from the top down, the first three modes are shown in Fig. 7 in a rectangular horizontal cross-section of the $2\pi \times \pi$ rectangular parallelepiped. Modes 1 and 3 have antisymmetric elevation (left) and symmetric velocity (right) fields, and vice versa for mode 2. The pictures present the following information. In the elevation field ζ (at the left), colouring and dashed lines represent elevation amplitudes. Deep blue corresponds with zero elevation, red with maximum amplitudes. Phase lines (every 30°) are solid. They end in nodal (zero elevation) points and show that phase is circling around the amphidromes in either clockwise or anticlockwise direction. All amphidromes on the middle axis ($y = \pi/2$) are traversed in a clockwise sense, all others (close to $y = 0$ and π) in anticlockwise sense. Orthogonal crossing of phase lines (as e.g. in the centre of the rectangle for mode 2) imply equal phases on all four branches, implying that the whole red central region of mode 2 rises and sinks in unison. Antisymmetry of the elevation field of e.g. mode 1 is evident from a 180° phase change between mirror images about the centre point.

The velocity field (u, v) (at the right-hand side of Fig. 7) contains, in principle, four independent parameters. Each component has an amplitude and a phase. At each individual location these can be represented in terms of a velocity ellipse, as e.g. in (Taylor, 1921), expressed in terms of four other parameters: maximum amplitude, $u_{\max}$, ellipticity $u_{\min}/u_{\max}$, orientation of the main axis, Ψ and phase (with respect to this local orientation) Φ (Prandle, 1982). The ellipticity varies between -1 (circular clockwise, deep blue), and $+1$ (circular anticlockwise, red), while it represents rectilinear motion when it is zero (green). The green colour at the boundary tells the velocity is rectilinear there. Separate consideration of the inclination shows the velocity vector to be everywhere parallel

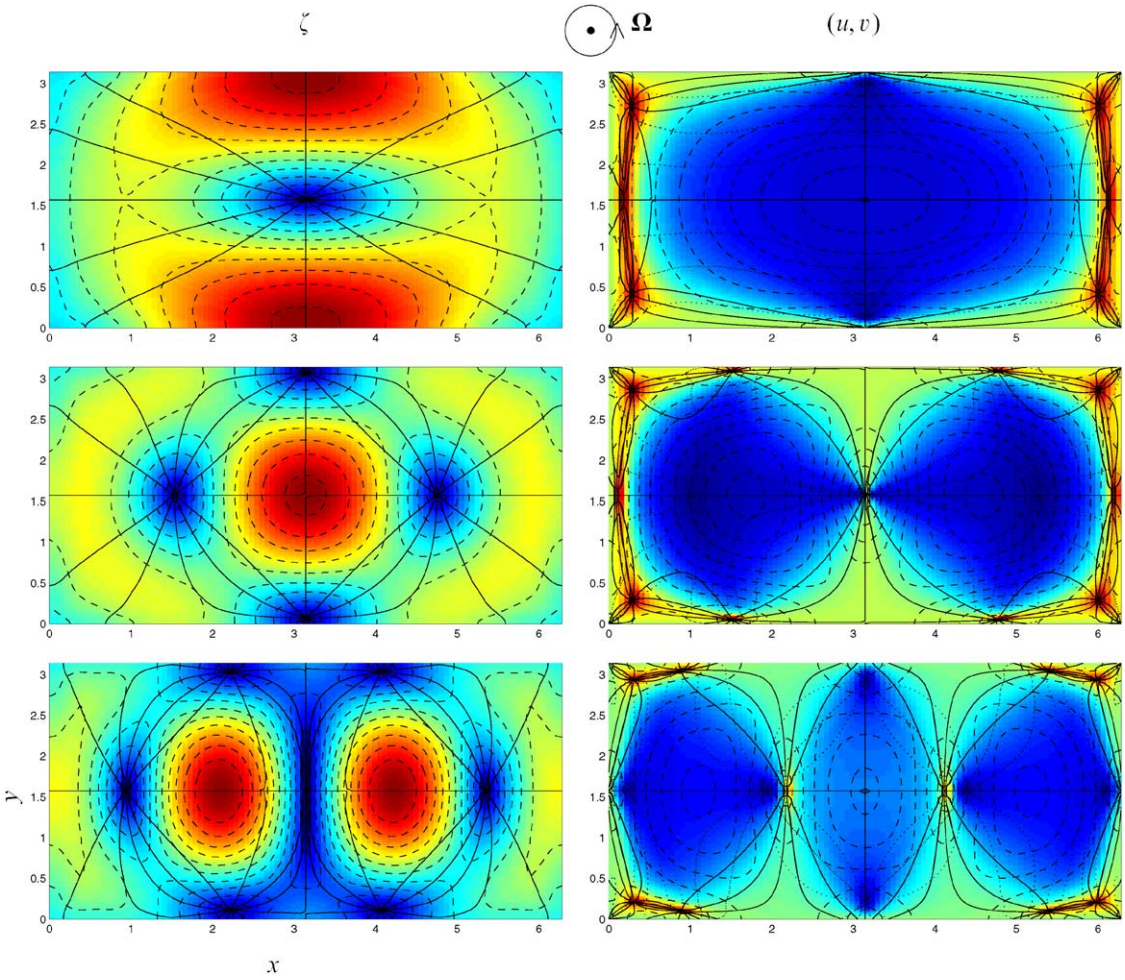

Fig. 7. Top view of elevation (left) and horizontal velocity (right) fields of a $2\pi \times \pi$ rectangle, for mode 1, $\sigma \approx 0.657$ (top); mode 2, $\sigma \approx 0.564$ (middle); and mode 3, $\sigma \approx 0.477$ (bottom). The rotation vector points out of the paper towards the reader; the tank thus moves anticlockwise. For further explanation, see main text.

to the sides. Maximum velocity ($u_{\max}$) is represented by dashed lines. Phase lines will be discussed below.

The Jth mode appears to have J cells of strong current maxima. These are each of a clockwise nature (negative ellipticities). At the sides, these are accompanied by a number of anticlockwise cells, separated by curves along which motion is rectilinear (zero ellipticity). Velocity amphidromes (locations where both $u = v = 0$) occur, of course, in the four corners of the basin, but may also occur elsewhere, as e.g. for mode 2, in the centre of the basin.

Each current ellipse can be viewed as the summation of two counterrotating circular currents of particular amplitude $W_{\pm}$ and phase $\theta_{\pm}$, of the same frequency as that of the mode considered (Prandle, 1982; Maas and van Haren, 1987). The positive sign refers to cyclonic (i.e. anticlockwise)

rotation of the current vector (and vice versa for negative sign). When the eigenvectors are found, working backwards through the definitions, also the horizontal velocity components are obtained, and can be written as $u = U_s \sin(\sigma t) + U_c \cos(\sigma t)$ and $v = V_s \sin(\sigma t) + V_c \cos(\sigma t)$, with the spatial amplitudes $(U, V)_{s,c}$ then known. The amplitudes $W_\pm$ and phases $\theta_\pm$ of the counterrotating velocity vectors are related to the Cartesian representations thereof, $W_{c\pm} = W_\pm \cos\theta_\pm$, and $W_{s\pm} = W_\pm \sin\theta_\pm$, themselves determined by $W_{c\pm} = (U_c \pm V_s)/2, W_{s\pm} = (V_c \mp U_s)/2$. When the counterrotating velocity vectors co-align, maximum current is obtained ($u_{max} = W_+ + W_-$); when they are in antiphase, the minimum current obtains ($u_{min} = W_+ - W_-$). Phase lines, $\theta_\pm$, circle around the nodes of the corresponding circular velocity amplitude fields; those of the clockwise ($-$) component (solid lines) around the deep red spots (where clockwise amplitude vanishes, $W_- = 0$), and those of the anticlockwise ($+$) component (dotted lines) around the deep blue spots (where $W_+ = 0$). The orientation and phase can then, as discussed above, in principle be obtained from these simply as $\Psi = (\theta_- + \theta_+)/2$ and $\Phi = (\theta_- - \theta_+)/2$. These are, of course, somewhat difficult to determine from the graphs and the definition of phase Φ, relative to the *local* orientation Ψ, renders this quantity somewhat less useful as a globally relevant parameter, which has therefore not been directly visualised here. However, the present graphs are useful in showing the intricate fine structure developing close to the walls, even for the lowest (i.e., highest frequency) modes. A similar sharp reversal of phase, close to the boundaries, can actually also be discerned in Taylor's solution of reflecting surface Kelvin waves (Taylor, 1921). Note that the phase is nearly constant in the blue cells, e.g. in the centre of the rectangle for the first mode. The deep blue color indicates that the ellipticity is dominated by the clockwise component, and the solid phase lines of this component are nearly uniformly zero. In other words, for mode 1, at time zero say, all currents in this blue area point towards positive y, and rotate clockwise at the same rate, in unison. The currents lead the elevation field by $\pi/2$ (zero phase for this mode being the horizontal line, to the left of the centre), but *lag* the vertical acceleration field, which drives the currents.

Comparing elevation and corresponding currents leads to the final observation that these fields act 'complementary', in the sense that where elevation field varies in phase, velocities have uniform phase, as the example of the first mode showed, *and* vice versa, as the elevation and currents of the second mode show near the centre of the tank. This implies that truly 3D amphidromes, $u = v = w(= -i\sigma\zeta) = 0$, have not been found in the interior.

Fig. 8 shows the same fields for the first 4 modes of the $\pi \times \pi$ square (so that, for the first vertical mode, the 3D box is a cube). Modes 1 and 4 correspond to v-symmetric modes, modes 2 and 3 to v-antisymmetric modes. Of course, the fields are all $x - y$ symmetric, although there is an interesting 'competition of symmetries' visible: the circular symmetry, reflecting the invariance of the governing equations to rotation, and the square symmetry, owing to the shape of the basin. The currents in the central amphidromes of modes 3 and 4 now turn anticlockwise, which is evident from the dominant anticlockwise (red) ellipticity, in the centre of the right lower two diagrams.

Another point of interest is the occurrence of a circle where phase lines cluster and the amplitude (nearly) vanishes (see elevation field of modes 2 and 4). This is reminiscent of the regular nodal lines occurring in *non-rotating* sloshing modes. Similar lines are visible in the velocity fields of modes 3 and 4 (where dotted phase lines cluster around circles of vanishing anticlockwise current component, $W_+ = 0$).

Another view of the velocity field can be offered by representing amplitudes and phases of the counterrotating circular components directly, as done in Fig. 9 for mode 4. Remarkably, the phase

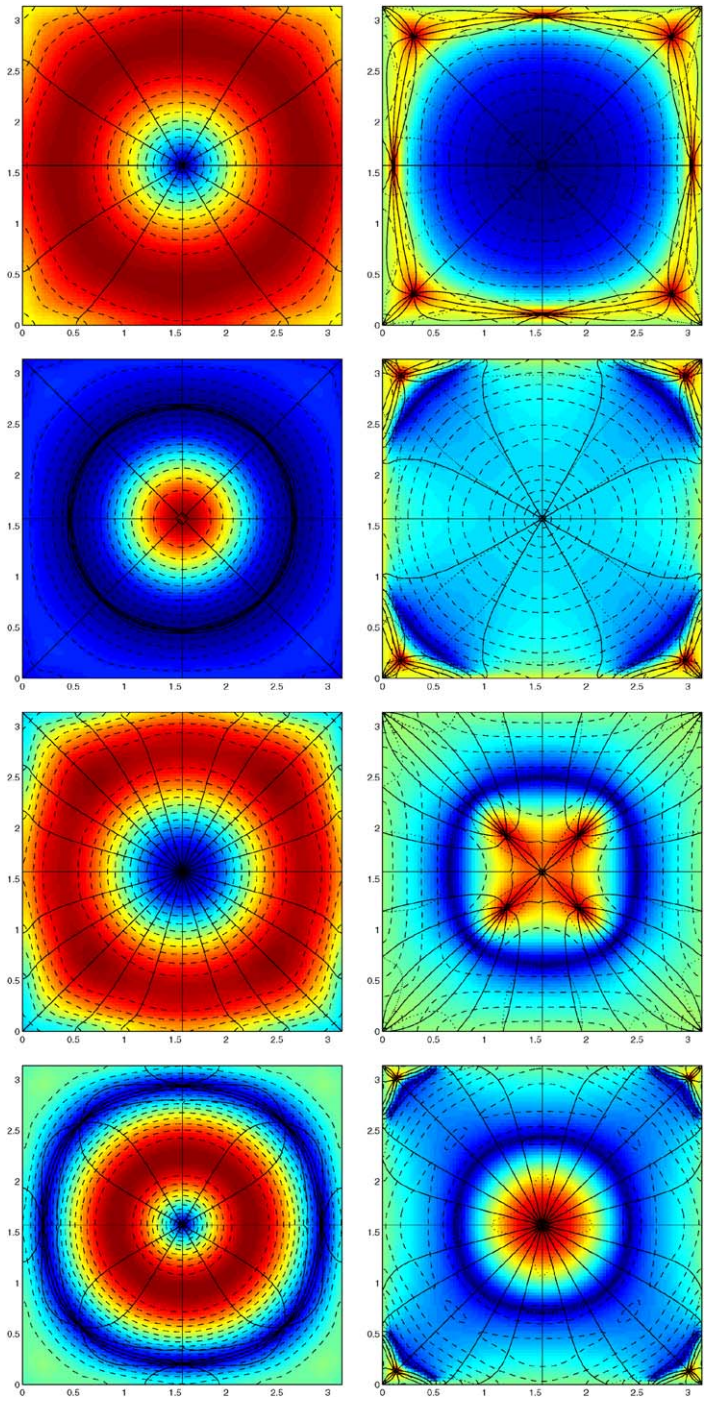

Fig. 8. As Fig. 7, for a $\pi \times \pi$ square. The eigenfrequencies of the first 4 modes are $0.547, 0.418, 0.369, 0.341$.

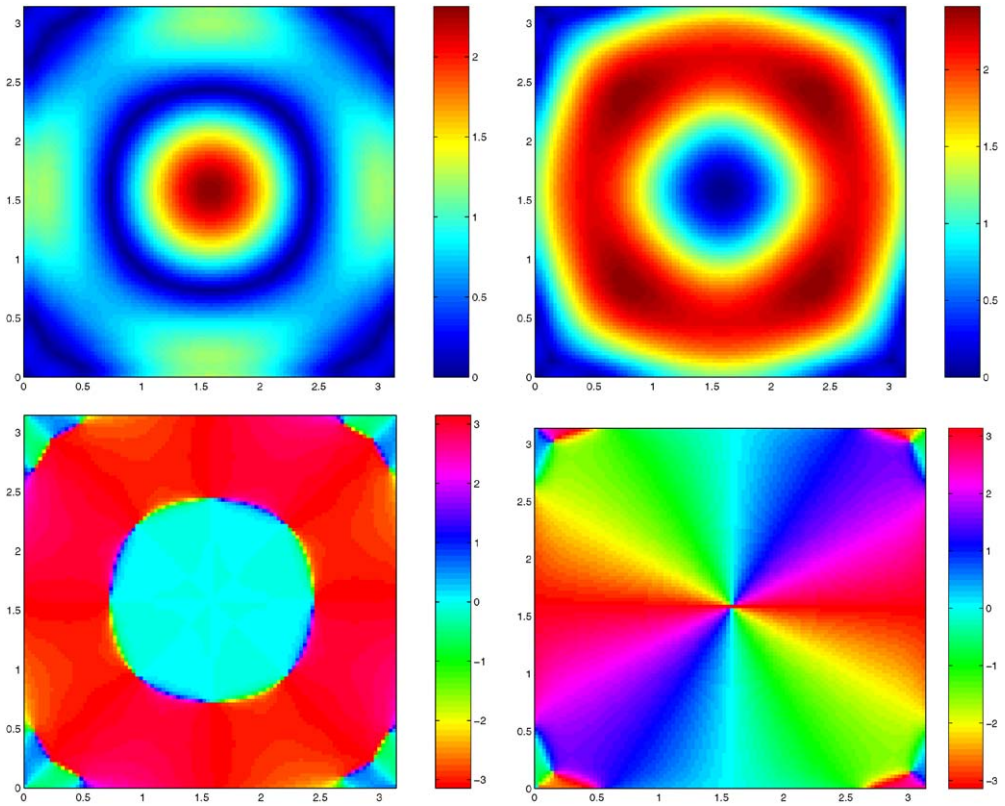

Fig. 9. Velocity amplitudes $W_{\pm}$ (top) and phases $\theta_{\pm}$ (bottom) of anticlockwise (+, left) and clockwise (−, right) rotating circular components of mode 4 in the $\pi \times \pi$ square.

of the anticlockwise (+) component (lower left) is nearly binary, which represents a sloshing mode, with a nodal (zero-amplitude) circle over which the phase 'jumps' $\approx 180°$. The clockwise (−) component, by contrast, shows a regular progression of phase. Amplitude patterns show a square symmetry, rotated over 45° with respect to each other, and are displaced radially. The corner regions are clearly locations of adjustment.

5. Summary and discussion

Rotating fluids support inertial waves, restored by Coriolis forces. Despite the concise way in which these waves can be described, very few fully confined geometries are known for which the governing, linearised equations have been completely solved. These are restricted to the axial can (with or without inner cylinder) (Kelvin, 1880), and the axial spheroid (Bryan, 1889) (of which only the subclass of toroidal modes survives in a spherical shell). To this we here add the horizontal rectangular parallelepiped. It is an interesting geometry, because it lacks the rotational symmetry which led to separable solutions in the previous containers. The present case is highly analogous to

that of rotationally modified, long surface gravity waves, studied at the beginning of the previous century (Poincaré, 1910; Proudman, 1916; Taylor, 1921). Equations quite similar to the long wave equations (governing these gravity waves) are obtained for each of the vertical modes that exist by virtue of non-hydrostatic effects in a fluid layer having top and bottom perpendicular to the rotation axis. In this case, vertical acceleration in the wave field replaces the acceleration of gravity, which is fully removed from the problem (by employing a reduced pressure). All reference to the particular vertical mode (n) is subsequently removed, since the depth scale of that mode ($H_*/n\pi$) can be used to scale the remaining equations. The resulting horizontal problem is solved in the unbounded domain, in the infinite and half-infinite channel, and in a fully contained rectangular parallelepiped, depending on the number of vertical walls (parallel to the rotation axis) that are added.

In the unbounded fluid layer it shows the existence of a continuum of plane low-frequency waves that are longer the closer they are to the inertial frequency ($2\Omega_*$). With one vertical boundary, two plane waves can be combined into the analog of Poincaré waves (here termed *inertial* Poincaré waves), such that the velocity component normal to this wall vanishes. This velocity component then vanishes also at a number of other lines, parallel to this wall, so that vertical walls can be fitted in there too and these waves constitute channel modes. Searching for inertial Kelvin (IK) waves, it is found that a decaying wave mode can be obtained, but it has particle motion in the direction of decay, making it incompatible with a solid boundary, so that free IK waves do not exist. During the reflection of channel inertial Poincaré waves from an end wall, however, such trapped waves do play a role, in combination with higher inertial Poincaré modes, which (above a certain mode number) are also trapped. In the final case, where another end wall is added, and we thus consider the waves in a rectangular parallelepiped, discretisation of the eigenfrequencies occurs. The wave system corresponding to each particular vertical mode, and each resulting eigenfrequency, can then either be cast as a combination of an infinite set of channel inertial Poincaré waves, together with two inertial Kelvin waves (Taylor's approach; results not shown here), or as a combination of two intertwined infinite sets of spatial Fourier modes (Proudman–Rao approach). The two approaches both lead to infinite matrix eigenvalue problems, which give similar results upon truncation of the matrices.

In line with the domain of infinite extent, eigenfrequencies creep up to the inertial frequency when the size is increased. This, of course, also occurs for the higher vertical modes, as the *apparent* domain size (the fixed length and width being scaled with the height scale of that mode) then increases. Varying the aspect ratio, paradoxically, a particular (infinite) discrete set of frequencies of the *infinitely long* channel seems to be favoured, namely that of modes having along-channel uniformity. While the particular mode associated with any of these eigenfrequencies varies with varying aspect ratio, that eigenfrequency persists. The resulting 'elevation' (vertical displacement) and horizontal velocity fields typically show amphidromic structures, where phase lines end in nodal (zero displacement, or velocity) points. The lowest modes show a complementarity of elevation and velocity fields, elevation fields lagging velocity fields (owing to the fact that vertical *acceleration* gradients drive the motion). In comparison to the surface gravity waves, maximum displacements (vertical velocities) now occur in the central portions of the fluid domain, not on the (vertical) boundaries. The waves sometimes take on a propagating form, sometimes a standing, sloshing form (as in the axial can). The overall impression is that of a central 'free' wave system (of multiple cells), to which 'wave boundary layers' are added in order to meet the impermeability requirements.

The existence of (linear) wave solutions does not guarantee their stability. Indeed, for the axial can the inertial waves (in this context often also referred to as Kelvin modes) were shown to be

actually *unstable* to short wavelength perturbations of oblique orientation (Lifschitz and Fabijonas, 1996, perhaps related to the observed resonance collapse (McEwan, 1970). Beautiful experiments exist in which the axial wall of the can is deformed elliptically, or triangularly, demonstrating how through triad interaction higher spatio-temporal modes and, in particular, also (zero frequency) steady patterns, like vortices and mean current structures are generated (Malkus, 1989; Eloy et al., 2000). Quite likely these stability results extend to the rectangular parallelepiped, considered here. Indeed, the resulting singularity (growth of amplitude of standing wave pattern, or development of small scales, Lifschitz and Fabijonas, 1996) is of precisely the same nature as that predicted when deformations of the container shape break the local reflectional symmetry (Maas, 2001). As argued in the introduction, focusing of wave energy (small scales) will then develop. When, however, some remaining symmetry exists, standing modes, consisting of strictly periodic characteristics (global resonances) may still occur, that will grow in amplitude when driven (Maas and Lam, 1995). While the observed focusing onto a rectangularly shaped attractor (in the experiment of Maas,2001), is correctly predicted with a 2D model, this yields no information of the structure of these waves on this 'wave attractor manifold' in the direction parallel to the slope, particularly with the presence of vertical end walls, to which, as in the present study, the circular currents have to adjust. We may speculate that the waves, once collapsed on this manifold, may still propagate along it, bearing perhaps some of the features of the present study, as e.g. amphidromes and near-uniformity in along-slope direction. Indeed, further observations (Manders and Maas, 2003) suggest a strong phase change in the velocity field occurring very close to the end wall, similar to that encountered in several of the low modes discussed here in the rectangular parallelepiped.

It is significant that associated with these wave-breakdowns, strong mean flows are often generated (Fultz, 1959; Thompson, 1979; Manasseh, 1996; Maas, 2001), perhaps the result of triad interaction, as discussed above, or due to mixing of fluid that is stratified in angular momentum, leading to the creation of shocks in the angular momentum profile, manifesting itself, in the rotating frame, as a mean flow (Maas, 2001).

Finally, the relevance of these type of waves to the natural environment is not clear-cut. Rotating water bodies as oceans and lakes are not only generally density-stratified, but even when they seem homogeneous, the weakest measurable stratification still often has stability frequencies in excess of the very weak inertial frequency (2Ω), associated with the rotation of the earth (van Haren et al., 1999). This serves to remind us that in nature waves in the hyperbolic wave regime generally occur as (internal) gravito-inertial waves. Only in convectively unstable circumstances (as in lakes and seas subject to intensive cooling (van Haren and Millot, 2003), or in the earth's liquid outer core), may the idealisation of an unstratified fluid arise naturally, and may the presently studied waves have some direct relevance (outside that in conditioned laboratory circumstances). With respect to that, perhaps also observations in the ocean's surface layer of a strong spectral peak, close to the critical frequency, and puzzlingly small horizontal scales thereof (of 20–10 km, e.g. (Fomin and Yampol'skiy, 1975; d'Asaro, 1984)), are not without significance. Despite their small-scale (order of the water depth) there seems to be no intrinsic reason to neglect these waves completely, such as enforced by the hydrostatic approximation (neglecting the left-hand side of Eq. (2.3)). Indeed, it is clear that the waves can get arbitrarily long close to, but just below the cut-off frequency $2\Omega_*$. Krauss (1973) observes that the hydrostatic approximation has been made ever since Laplace, but that a real motivation (except for the tautological statement that it applies to waves that are long compared with water depth) is absent. Indeed, for this reason the approximation has been criticized

by Solberg (1936), when looking into these inertial 'cellular' waves, and it was argued to, moreover, destroy the notion of wave attractors (Maas, 2001). The failure of Laplace's Tidal Equations to even adequately model long surface waves in the presence of topographic variations was addressed by Chapman (1982), and Chapman and Hendershott (1982).

Indirectly, this study may however be of relevance for elucidating the structure of contained gravito-inertia waves, as it is again rotation that will provide a coupling between the otherwise separable Fourier modes. This will not alleviate the need to consider the fact that in any natural container the delicate local reflectional symmetry, of the 'horizontal' container employed here, will be broken, which requires determining the wave structure on 3D attractors, possibly endowed with amphidromic structures and 'wave boundary layers', and its contribution relative to that of other supported wave modes (as Rossby waves).

Acknowledgements

The author is grateful to Theo Gerkema for making perceptive comments on a first draft.

Appendix. Internal gravity waves in a rectangular parallelepiped

In a non-rotating, uniformly stratified (constant stability frequency N) fluid, the spatial structure of the pressure field of monochromatic internal gravity waves of frequency σ ($0 \leqslant \sigma \leqslant N$) is again governed by a hyperbolic equation

$$p_{xx} + p_{yy} - \left(\left(\frac{N}{\sigma} \right)^2 - 1 \right)^{-1} p_{zz} = 0. \tag{5.1}$$

This follows from the momentum equations and material conservation of density, leading to $\mathrm{i}\sigma(u, v, w(1 - N^2/\sigma^2)) = \nabla p$, together with incompressibility. For these waves, however, the impermeability condition ($\mathbf{u} \cdot \mathbf{n} = 0$), at walls that are either parallel or perpendicular to gravity, is simply a Neumann condition, requiring the vanishing of the normal pressure gradient $\partial p/\partial n$ at each of these walls. For the rectangular parallelepiped (of size $H \times L_x \times L_y$) this implies the existence of separable solutions,

$$p = p_{kln} \cos k\pi x/L_x \cos l\pi y/L_y \cos n\pi z/H \tag{5.2}$$

for integer k, l, n, satisfying the equation and boundary conditions with undetermined amplitudes p_{kln}, provided the wave numbers relate to the frequency by

$$\frac{\sigma}{N} = \left(1 + \frac{(n/H)^2}{(k/L_x)^2 + (l/L_y)^2} \right)^{-1/2}. \tag{5.3}$$

Clearly, if the original (k, l, n) is replaced by $(k', l', n') = j(k, l, n)$, this leaves the eigenfrequency unaffected, and for integer j, also the boundary conditions. The eigenfrequency is therefore (infinitely) degenerate. A second degeneracy exists for rational aspect ratios $L_y/L_x = q/r$, where q, r are co-prime.

Replacing the original (k,l,n) by (k',l',n'), with $k'=r^2l$, $l'=q^2k$, and $n'=rqn$, again leaves the eigenfrequencies unchanged. (For square basins this simply comes down to an exchange $k \leftrightarrow l$.) These two independent degeneracies suggest that the 2D notion of a fundamental interval, over which an arbitrarily prescribed pressure uniquely determines the amplitudes of the Fourier coefficients (Maas and Lam, 1995), carries over to the 3D case in the existence of a fundamental *area*. In the 2D case, the pressure values in the fundamental interval also uniquely defined the partial pressures carried invariantly along each periodic web of connected characteristics, thus providing an exact alternative (and, in fact, more general) representation of the solution. As the characteristics in 3D are conical blades, the analogy between the Fourier representation on the one hand, and a beam-wise representation is here not as clearcut and requires further investigation.

References

Aldridge, K.D., Toomre, A., 1969. Axisymmetric oscillations of a fluid in a rotating spherical container. J. Fluid Mech. 37, 307–323.

Bai, Z., Sleijpen, G., van der Vorst, H., 2000. Quadratic and nonlinear eigenproblems. In: Bai, Z., Demmel, J., Dongarra, J., Ruhe, A., van der Vorst, H. (Eds.), Templates for the Solution of Algebraic Eigenvalue Problems: A Practical Guide. SIAM, Philadelphia, PA.

Bäuerle, E., 1998. Excitation of internal seiches by periodic forcing. In: Imberger, J. (Ed.), Physical Processes in Lakes and Oceans, Coastal and Estuarine Studies, Vol. 54. American Geophysical Union, Washington, DC, pp. 167–178.

Beardsley, R.C., 1970. An experimental study of inertial waves in a closed cone. Stud. Appl. Math. 49, 187–196.

Berry, M.V., 1987. Quantum chaology. Proceedings of the Royal Society of London A, Vol. 413, pp. 183–198.

Bjerknes, V., Bjerknes, J., Solberg, H., Bergeron, T., 1933. Physikalische Hydrodynamik. Springer, Berlin.

Brekhovskikh, L.M., Goncharov, V., 1993. Mechanics of Continua and Wave Dynamics, 2nd Edition. Springer, Berlin.

Bryan, 1889. The waves on a rotating liquid spheroid of finite ellipticity. Philos. Trans. Roy. Soc. London 180, 187–219.

Cartan, M.E., 1922. Sur les petites oscillations d'une masse fluide. Bull. Sci. Math. 46, 317–369.

Cartwright, D., 1999. Tides, a Scientific History. Cambridge University Press, Cambridge.

Chapman, D., 1982. On the failure of Laplace's tidal equations to model subinertial motions at a discontinuity in depth. Dyn. Atmos. Oceans 7, 1–16.

Chapman, D., Hendershott, M., 1982. Shelf wave dispersion in a geophysical ocean. Dyn. Atmos. Oc. 7, 17–31.

d'Asaro, E.A., 1984. Wind forced internal waves in the north pacific and sargasso sea. J. Phys. Oceanogr. 14, 781–794.

deWitt, L.M., Levine, M.D., Paulson, C.A., Burt, W.V., 1986. Semidiurnal internal tide in jasin: observations and simulation. J. Geophys. Res. 91, 2581–2592.

Eloy, C., Gal, P.L., Dizès, S.L., 2000. Experimental study of the multipolar vortex instability. Phys. Rev. Lett. 85, 3400–3403.

Fomin, L.M., Yampol'skiy, A.D., 1975. Vertical structure of inertial motions in the sea. Oceanology, Engl. Transl. 15, 21–26.

Fu, L.L., 1981. Observations and models of inertial waves in the deep ocean. Rev. Geophys. Space Phys. 19, 141–170.

Fultz, D., 1959. A note on overstability and the elastoid-inertia oscillations of kelvin, solberg and bjerknes. J. Meteorol. 16, 199–208.

Gerkema, T., 2001. Internal and interfacial tides: beam scattering and local generation of solitary waves. J. Mar. Res. 59, 227–255.

Görtler, H., 1944. Einige bemerkungen über strömungen in rotierenden flüssigkeiten. Z. Angew. Math. Mech. 24, 210–214.

Greenspan, H., 1968. The Theory of Rotating Fluids. Cambridge University Press, Cambridge.

Hendershott, M.C., 1981. Long waves and ocean tides. In: Warren, B.A., Wunsch, C. (Eds.), Evolution of Physical Oceanography. MIT Press, Cambridge, MA.

Høiland, E., 1962. Discussion of a hyperbolic equation relating to inertia and gravitational fluid oscillations. Geofys. Publ. 24, 211–227.

Hutter, K., 1993. Waves and oscillations in the ocean and in lakes. In: Hutter, K. (Ed.), Continuum Mechanics in Environmental Sciences and Geophysics, CISM Courses and Lectures, No 337. Springer, Wien, New York, pp. 79–240.
Kelvin, L., 1880. Vibrations of a columnar vortex. Philos. Mag. 10, 155–168.
Kerswell, R.R., 1995. The instability of precessing flow. Geophys. Astrophys. Fluid Dyn. 303, 233–252.
Kobine, J.J., 1995. Inertial wave dynamics in a rotating and precessing cylinder. J. Fluid Mech. 303, 233–252.
Krauss, W., 1973. Methods and results of theoretical oceanography I, Dynamics of the homogeneous and the quasihomogeneous ocean. Gebr. Borntraeger.
Küchemann, D., 1965. Inertial wave dynamics in a rotating and precessing cylinder. J. Fluid Mech. 21, 1.
Lamb, S.H., 1932. Hydrodynamics, 6th Edition. Dover, New York.
LeBlond, P.H., Mysak, L.A., 1978. Waves in the Ocean. Elsevier, Amsterdam.
Lifschitz, A., Fabijonas, B., 1996. A new class of instabilities of rotating fluids. Phys. Fluids 8, 2239–2241.
Lighthill, S.M.J., 1966. Dynamics of rotating fluids: a survey. J. Fluid Mech. 26, 411–431.
Maas, L.R.M., 2001. Wave focusing and ensuing mean flow due to symmetry breaking in rotating fluids. J. Fluid Mech. 437, 13–28.
Maas, L.R.M., Lam, F.P.A., 1995. Geometric focusing of internal waves. J. Fluid Mech. 300, 1–41.
Maas, L.R.M., van Haren, J.J.M., 1987. Observations on the vertical structure of tidal and inertial currents in the central North Sea. J. Mar. Res. 45, 293–318.
Maas, L.R.M., Benielli, D., Sommeria, J., Lam, F.-P.A., 1997. Observation of an internal wave attractor in a confined stably-stratified fluid. Nature 388, 557–561.
Malkus, W.V.R., 1967. Hydromagnetic planetary waves. J. Fluid Mech. 28, 793–802.
Malkus, W.V.R., 1968. Precession of the earth as the cause of geomagnetism. Science 160, 259–264.
Malkus, W.V.R., 1989. Geophys. Astrophys. Fluid Dyn. 48, 123.
Manasseh, R., 1992. Breakdown regimes of inertia waves in a precessing cylinder. J. Fluid Mech. 243, 261–296.
Manasseh, R., 1994. Distortions of inertia waves in a rotating fluid cylinder forced near its fundamental mode resonance. J. Fluid Mech. 265, 345–370.
Manasseh, R., 1996. Nonlinear behaviour of contained inertia waves. J. Fluid Mech. 315, 151–173.
Manders, A., Maas, L.R.M., 2003. Observations of inertial waves in a rectangular basin with one sloping boundary. J. Fluid Mech., in press.
McEwan, A.D., 1970. Inertial oscillations in a rotating fluid cylinder. J. Fluid Mech. 40, 603–640.
McEwan, A.D., 1971. Degeneration of resonantly-excited standing internal gravity waves. J. Fluid Mech 50, 431–448.
Mortimer, C.H., 1974. Lake hydrodynamics. Mitt. Int. Ver. Limnol. 20, 124–197.
Oser, H., 1958. Experimentele untersuchung über harmonische schwingungen in rotierenden flüssigkeiten. Z. Angew. Math. Mech. 38, 386–391.
Phillips, O.M., 1963. Energy transfer in rotating fluids by reflection of inertial waves. Phys. Fluids 6, 513–520.
Poincaré, H., 1885. Sur l'équilibre d'une masse fluide animée d'un mouvement de rotation. Acta Math. VII, 259–380.
Poincaré, H., 1910. Sur la précession des corps déformables. Bull. Astronom. 27, 321.
Prandle, D., 1982. The vertical structure of tidal currents. Geophys. Astrophys. Fluid Dyn. 22, 29–49.
Proudman, J., 1916. On the dynamical theory of tides. Part ii. flat seas. Proceedings of the London Mathematical Society, 2nd Series, Vol. 18, pp. 21–50.
Rao, D., 1966. Free gravitational oscillations in rotating rectangular basins. J. Fluid Mech. 25, 523–555.
Rieutord, M., Georgeot, B., Valdettaro, L., 2000. Wave attractors in rotating fluids: a paradigm for ill-posed Cauchy problems. Phys. Rev. Lett 85, 4277–4280.
Scott, W.E., 1974. The large amplitude motion of a liquid-filled gyroscope and the non-interaction of inertial and rossby waves. J. Fluid Mech. 72, 649–660.
Solberg, H., 1936. über die freien schwingungen einer homogenen flüssigkeitsschicht auf der rotierenden erde. i. Astrophys. Norv. 1, 237–340.
Taylor, G.I., 1921. Tidal oscillations in gulfs and basins. Proceedings of the London Mathematical Society Series 2, Vol. XX, pp. 148–181.
Thompson, R.O.R.Y., 1979. A mechanism for angular momentum mixing. Geophys. Astrophys. Fluid Dyn. 12, 221–234.
Tolstoy, I., 1973. Wave Propagation. McGraw-Hill, New York.

van Haren, J.J.M., Maas, L.R.M., Zimmerman, J.T.F., Ridderinkhof, H., Malschaert, H., 1999. Strong inertial currents and marginal wave stability in the central north sea. Geophys. Res. Lett. 26, 2993–2996.

van Haren, H., Millot, C., 2003. Rectilinear and circular inertial motions in the Western Mediterranean Sea. Oceanol. Acta, in press.

Vanyo, J., Wilde, P., Cardin, P., Olson, P., 1995. Experiments on precessing flows in the earth's liquid core. Geophys. J. Int. 121, 136–142.

Whewell, 1833. Essay towards a first approximation to a map of cotidal lines. Philos. Trans. Roy. Soc. London 123, 147–236.

Wood, W., 1966. An oscillatory disturbance of rigidly rotating fluid. Proceedings of the Royal Society of London A, Vol. 293, pp. 181–212.

Yamagata, 1978. Wave-induced boundary layers in a rotating homogeneous fluid. J. Oceanogr. Soc. Japan 34, 97–104.